Charged-particle spectra: 80 MeV deuterons on ^{27}Al and ^{58}Ni and 70 MeV deuterons on ^{90}Zr, ^{208}Pb, and ^{232}Th

J. R. Wu, C. C. Chang, and H. D. Holmgren

Department of Physics and Astronomy, University of Maryland, College Park, Maryland 20742

(Received 1 February 1978)

Complete energy spectra and angular distributions of charged light particles ($Z \leq 2$ and $A \leq 4$) were measured for the bombardment of 80 MeV deuterons on ^{27}Al and ^{58}Ni and 70 MeV deuterons on ^{90}Zr, ^{208}Pb, and ^{232}Th. The charged particles were detected by two triple-counter telescopes using combinations of ΔE-E and time-of-flight techniques for particle identification. The experimental results are presented in cross sections doubly differential in energy and angle, as well as in angle- and energy-integrated cross sections. For all the nuclei studied, the proton energy spectra show large deuteron-breakup peaks centered at approximately half of the incident deuteron energy at forward angles. The energy spectra for the same type of emitted particle are similar in shape for all nuclei at a given angle except in the region of the low-energy evaporation peak. The magnitude of evaporation peak varies rapidly with target mass. The total nonequilibrium yield of charged light particles is approximately $(300 \pm 50)A^{1/3}$mb. The angular distributions for the high-energy particles are strongly forward peaked and are nearly isotropic for the low-energy particles. The deuteron and triton yields increase with A; while those for p, ^{3}He, and α particles decrease with A. The total charged light-particle yield is found to be roughly two times the total reaction cross section (σ_R) for light- and medium-mass nuclei; while it is less than σ_R for heavy nuclei. The experimental results were analyzed within the framework of the pre-equilibrium exciton model together with evaporation theory. The pre-equilibrium exciton model using a 3p-1h initial configuration reproduces the experimental angle-integrated energy spectra for all target nuclei studied both in spectral shapes and in magnitudes for all emitted particles except protons. The deuteron-breakup yield in the proton spectra was compared with the Serber model. When the breakup yield is added to the pre-equilibrium yield, agreement is obtained for the proton spectra.

$$\left[\begin{array}{l} \text{NUCLEAR REACTIONS } {}^{27}\text{Al, } {}^{58}\text{Ni, } {}^{90}\text{Zr, } {}^{208}\text{Pb, } {}^{232}\text{Th } (d,xp), \ (d,xd), \ (d, \ xt), \\ (d, \ x^{3}\text{He}), \ (d,x\alpha), \ E = 80, \ 70 \ \text{MeV}; \ \theta = 20° \text{--} 150°, \ \text{measured } d^{2}\sigma/d\Omega d\epsilon, \ \text{deduced} \\ d\sigma/d\epsilon \text{ and } \sigma(E). \ \text{Comparisons with pre-equilibrium exciton, compound nuclear} \\ \qquad\qquad\qquad \text{evaporation and deuteron–breakup models.} \end{array} \right]$$

I. INTRODUCTION

In the energy region above 50 MeV, the wavelength of an incident nucleon becomes comparable to nuclear dimensions. The influence of nucleon-nucleon interactions begins to be manifested and their effects become more apparent with increasing energy. We expect the effects of multiple scattering to dominate nucleon-induced nuclear reactions in the energy range from 50 to 150 MeV. For energies above 150 MeV the single nucleon-nucleon collision becomes the dominant interaction.[1]

In the energy region between 50 and 150 MeV, models of nuclear reactions involving two stages have often been used. The incident nucleon is first assumed to interact with the target nucleus by a series of nucleon-nucleon collisions initiating a nuclear cascade. During the nuclear cascade, one or more high-energy particles may be ejected, leaving the residual nucleus in an excited state. Second, the residual excited nucleus may deexcite by emitting additional particles or γ rays. The

general description of the interaction of a particle with a nucleus emphasizing the early multiple collision process has been called the pre-equilibrium reaction.

Many different approaches have been developed to interpret such reactions. Among them are the intranuclear cascade model (INC),[2] the quasi-free scattering model (QFS),[3] the pre-equilibrium exciton model (PE),[4] and the hybrid model.[5] These various models have been reasonably successful in accounting for a large body of experimental data.

Conceptually, the pre-equilibrium process for nucleon emission is straightforward. The processes for complex particle emission are, however, not as clear. Experimental information using composite particles as projectiles at higher energies as well as the observation of the emission of complex particles are required in order to understand more completely the dominant nuclear reaction mechanisms.

From the experimental point of view, the multi-particle-removal reactions can be studied either

by measuring the cascade γ rays[6] which are used to identify the residual nuclei or by observing the complete energy spectra of emitted particles from which the dominant nuclear reaction mechanisms can be studied. Most of the measurements of the particle spectra have concentrated on the proton or α particle channels, and were carried out at relatively low energies.[7] Less attention has been directed toward the study of other complex particles either in the incident or the exit channels, although measurements have been carried out at 62 MeV for proton-induced reactions.[8]

Deuteron-induced reactions have been rarely explored in the energy range above 50 MeV. The availability of deuteron beams with energies up to 80 MeV at the University of Maryland allows us to investigate a number of interesting nuclear reactions. Most nuclear structure experiments using deuterons have emphasized only the low-lying discrete states[9] or the giant resonance regions of the spectra.[10] Little attention has been directed toward the measurement of entire energy spectra, extending from a few MeV up to maximum kinematically allowed energy, except for some investigations made at lower energy.[11-13] The results of the nucleon-induced or α-induced reactions at energies above 10 MeV indicate that exit channels other than the entrance channels also represent a large yield.[7,8] It is, therefore, important to obtain complete experimental information on charged-particle production induced by complex projectiles at higher energies.

In this work, we have concentrated on the measurements of the complete charged-particle energy spectra using 70 MeV and 80 MeV deuterons on five nuclei spanning the periodic table. Briefly, the objectives of this investigation are

(1) To study the dominant reaction mechanisms which produce the energy and angular dependence of the observed spectra of charged particles.

(2) To study how the reaction cross section is distributed among the various reaction channels.

(3) To study the dependence of the charged-particle yields on target nuclei.

(4) To test the validity of the existing models. We have limited ourselves to the pre-equilibrium exciton model and the deuteron-breakup model.[14]

(5) To obtain information about complex particle formation.

(6) To provide guidance for further theoretical development.

In Sec. II, the experimental method is described. In Sec. III, the data are presented in the forms of differential energy spectra $[d^2\sigma/d\Omega d\epsilon$ (mb/sr MeV)], angle-integrated energy spectra $[d\sigma/d\epsilon$ (mb/MeV)], angular distributions for different energy bins $[d^2\sigma/d\Omega d\epsilon$ (mb/sr MeV)], integral particle production yield $[\sigma_\beta(E)$ (mb)], total charged-particle pro- duction yield $[\sigma_t(E)$ (mb)], and the mean yield or multiplicity of particle β, i.e., $Y_\beta = \sigma_\beta(E)/\sigma_R(E)$, where $\sigma_R(E)$ is the total reaction cross section. In Sec. IV, the experimental data were analyzed in the framework of pre-equilibrium exciton model, compound nuclear evaporation model and the Serber model of deuteron breakup.

II. EXPERIMENTAL METHOD

The University of Maryland sector focused isochronous cyclotron provides good energy resolution and high duty cycle deuteron beams with energies up to 80 MeV. In this series of experiments, the energy spectra of secondary proton, deuteron, triton, ^{3}He, and α particles were measured with 70 MeV deuterons on ^{90}Zr, ^{208}Pb, ^{232}Th and 80 MeV deuterons on ^{27}Al and ^{58}Ni. The spectra were obtained at approximately ten angles from 20° to 150° in 15° steps. The typical energy resolution of the beam transported to the scattering chamber was approximately 40 keV. The beam currents used varied from 10 to 200 na, depending upon the angle of observation and the target. The beam spot size on target was ~2mm×2mm. The experiments were carried out in a high resolution and low background experimental area. The beam was first momentum analyzed through two 90°-bend analyzing magnets and then bent additional 20° through a switching magnet. Many sets of "clean up" slits were placed between magnets. The slit widths were adjusted to minimize the scattering of beam halo from the target frame by use of a blank target and with the detectors located at small angles. Although no attempt was made to measure the low-energy component of the beam, this component was believed to be small due to the beam transport system described above.

The target thickness was generally limited because of the need to observe low-energy helium ions. Five targets spanning the periodic table were investigated: ^{27}Al(1.72 mg/cm^2), ^{58}Ni(1.11 mg/cm^2), ^{90}Zr(5.8 mg/cm^2), ^{208}Pb(3 mg/cm^2), and ^{232}Th(1.03 mg/cm^2). A CH target was used to provide an energy calibration for the emitted hydrogen particles by observing deuterons scattered from ^{12}C and the recoiled protons at various angles.

The primary interest of this experiment was to measure the charged light-particle ($Z \leq 2, A \leq 4$) energy spectra over the entire energy range of particles produced by 70 and 80 MeV deuterons on the above targets. Two triple-counter telescopes were employed to compensate the gaps which appeared in the spectrum due to detector dead layers and electronic thresholds in each telescope. One counter telescope was capable of stopping the highest-energy hydrogen particles and the other, the maximum-energy helium particles. The choice of
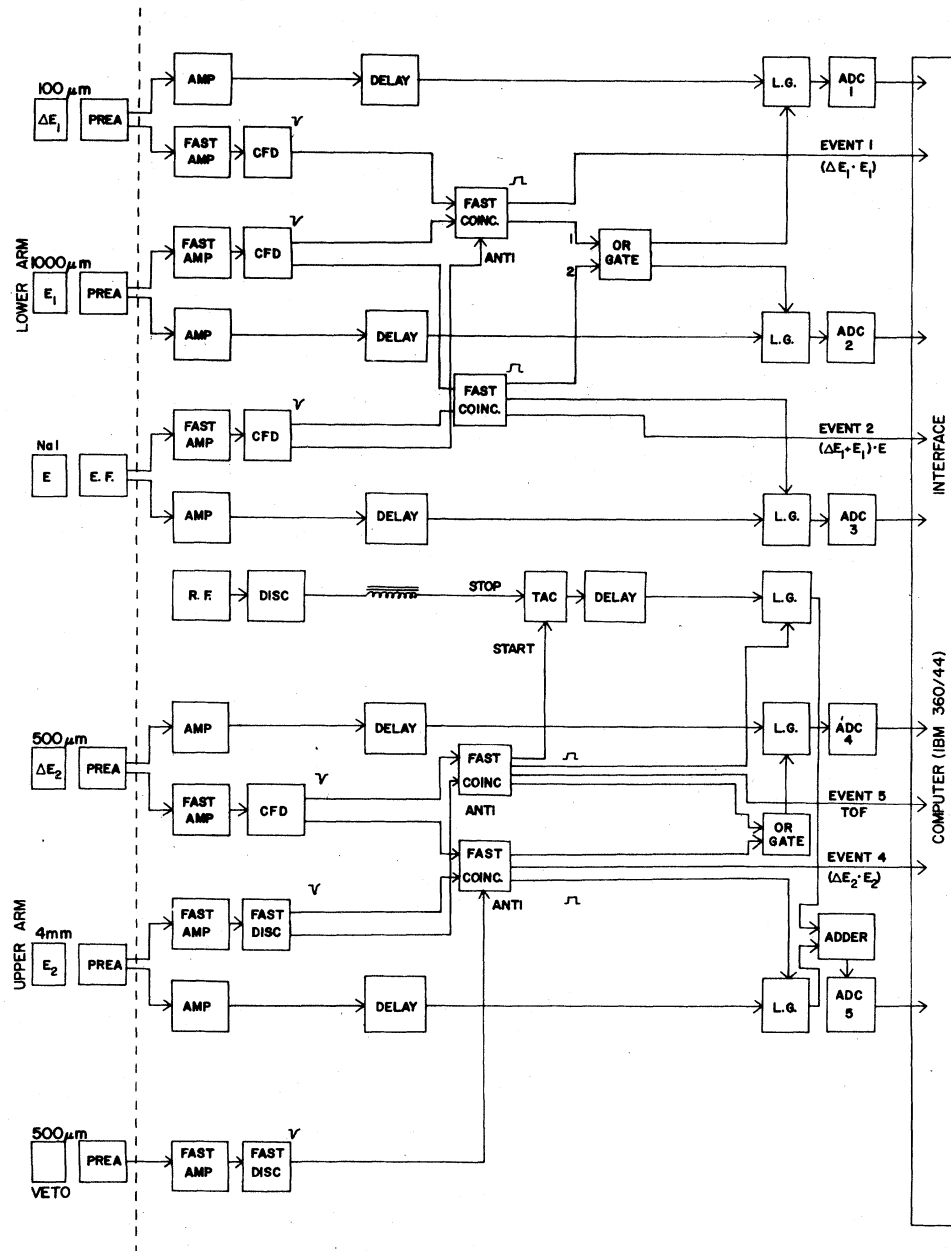
FIG. 1. The electronics block diagram.

the detector thickness and detector type was deter-
mined by the following factors: (1) to provide good
particle identification, (2) to stop high-energy par-
ticles, and (3) to identify tritons and ^{3}He to as low
an energy as possible [these particles cannot be
separated by time of flight (TOF) information].
The two telescopes were (1) 100 μm(Si)—1000 μm
(Si)—7.6 cm NaI, and (2) 500 μm(Si)—4000 μm
(Si-Li)—500 μm(Si). The detector solid angles
were 0.27 and 0.23 msr, respectively. The over-
all energy resolution of the energy spectrum ob-

tained with NaI was about 400 keV.

The secondary particles were identified by a com-
bination of $\Delta E \cdot E$ and (TOF) vs E techniques which
permitted unambiguous particle identification over
an energy range from a few MeV to a maximum
energy which was kinematically allowed for particle
with $A \leq 4$. Information was also obtained for par-
ticles with $A > 5$ in the form of two-dimensional
spectra of TOF vs E.

All Si detectors were calibrated using a ^{228}Th α
source. The NaI detector was calibrated by ob-

serving the spectrum from the CH target resulting from the 70 or 80 MeV deuteron beams.

A block diagram of the electronic setup used in this experiment is shown in Fig. 1. The setup includes a fast-logic system, a linear-pulse-height analysis system, and a computer-interface system (IBM 360/44). Outputs from the first two systems were combined in the third for on line processing, storage, and display. Two events were associated with each counter telescope for particle identification: $\Delta E_1 \cdot E_1$, $(\Delta E_1 + E_1) \cdot E$, TOF vs ΔE_2, and $\Delta E_2 \cdot E_2$. Note that the computer software summed ΔE_1 and E_1 as ΔE for the second event. The beam arrival time relative to the RF signal was monitored and the TOF was corrected to about 1 ns. The details of the electronics, computer software, and data taking procedures are described in Ref. 15 and references therein.

A complete particle spectrum was constructed from sections of the spectra corresponding to the four different events used to identify the particle type. No cross normalization for each section was made because each triple-counter telescope was normalized separately. The spectra were corrected for the reaction tails produced in the detector, collimator scattering, energy loss, and straggling in the target, low-energy background arising from target contaminants, and background contributed from the beam. The spectra were then summed into 1 MeV energy bins to provide smoother curves. For more detailed treatment of the data, see Ref. 15.

The differential cross sections were transformed to the c.m. system using the relationship

$$\frac{1}{p'}\frac{d^2\sigma'(\theta')}{d\Omega'd\epsilon'} = \frac{1}{p}\frac{d^2\sigma(\theta)}{d\Omega d\epsilon}, \qquad (1)$$

where p and p' are the momenta of emitted particles in the laboratory and the c.m. systems, respectively. The assumption was made that all

TABLE I. Summary of the experimental conditions and measured integral cross sections.

Target and incident energy	Compound nucleus and initial excitation energy	Angles observed (degree)	Particle emitted	Low energy cutoff (MeV)	Reaction Q value (MeV)	Measured average emitted energy (MeV) $\bar{E}$	Average low energy peak location (MeV)	Calculated Coulomb barrier (MeV) a	Measured integral cross section in lab σ_t (mb) b
^{27}Al $E_d = 80$ MeV	^{29}Si $E^* = 92.28$ MeV	30, 45, 60, 90, 120, 135, 150.	p d t ^{3}He ^{4}He	2 2 5.5 11 2	5.50 0 −6.79 −2.79 6.69	20.44 50.20 30.26 37.45 11.11	3.5 4.5 6.5 ••• 4.5	3.12 2.93 2.83 5.23 5.11	1651 ± 165
^{58}Ni $E_d = 80$ MeV	^{60}Cu $E^* = 88.55$ MeV	20, 30, 45, 60, 90, 120, 135, 150.	p d t ^{3}He ^{4}He	2 3 5.5 11.5 2	6.77 0 −5.94 −2.70 6.51	16.81 38.51 32.62 35.79 13.69	4.5 6.5 6.5 ••• 8.5	5.49 5.24 5.08 9.80 9.58	3526 ± 350
^{90}Zr $E_d = 70$ MeV	^{92}Nb $E^* = 79.25$ MeV	20, 30, 45, 60, 90, 120, 135, 150.	p d t ^{3}He ^{4}He	2 3 5.5 12 3	4.96 0 −5.74 −2.90 6.21	19.95 37.07 30.39 29.53 15.03	6.5 ••• 7.5 ••• 11.5	6.98 6.69 6.50 12.68 12.41	2365 ± 240
^{208}Pb $E_d = 70$ MeV	^{210}Bi $E^* = 75.50$ MeV	20, 30, 45, 60, 75, 90, 105, 120, 140.	p d t ^{3}He ^{4}He	5 5 5.5 11.5 14	1.71 0 −1.12 −2.56 11.21	34.07 49.19 34.03 44.60 31.46	••• ••• 15.5 ••• 23.0	11.35 10.96 10.70 21.14 20.75	2112 ± 210
^{232}Th $E_d = 70$ MeV	^{234}Pa $E^* = 77.71$ MeV	20, 30, 45, 60, 75, 105, 120, 140.	p d t ^{3}He ^{4}He	6 6 6 11.5 14	2.73 0 −0.11 −2.20 12.45	35.29 49.33 31.19 39.07 31.04	••• 19.5 17.5 ••• 23.0	12.08 11.67 11.40 22.55 22.15	2013 ± 200

a Coulomb barriers are calculated from $V_c = 1.44zZ/1.5(A^{1/3} + a^{1/3})$.

b Excluding the elastic scattering.

observed particles were emitted from a nucleus moving with initial c.m. velocity.

The cross sections integrated over either laboratory or c.m. angles,

$$d\sigma/d\epsilon = 2\pi \int_0^\pi \frac{d^2\sigma}{d\Omega d\epsilon} \sin\theta\, d\theta ,$$

were obtained by means of Gauss integration. For integration purposes, the Lagrange interpolation/extrapolation method was employed to estimate the cross section of those integration points which fall outside the experimental data.

The uncertainties in the experimental cross sections arise from the solid angle (~1%), the statistical error which could be as large as 20% for high-energy triton, ^{3}He, and α particles, the target thickness (<5%), the integrated beam current (<0.3%), the background from slit scattering (<1%), and the uncertainties due to various corrections (<5%). Additional uncertainties may also have resulted from mixing one particle type into another as a result of gain shift, the electronics dead time, and the contaminants. However, these were considered to be small. In obtaining the angle-integrated cross section and c.m. transformation, additional uncertainties might also arise due to the propagation of the statistical error in the extrapolation/interpolation. The overall error is ~10%.

III. EXPERIMENTAL RESULTS AND DISCUSSION

Table I summarized the targets studied, the incident projectile energies, the compound system, the initial excitation energy, angles of observation, the low-energy cutoff for each particle observed, reaction Q value, average emitted energy measured, average observed low-energy peak location, calculated Coulomb barrier, and the measured integral charged particle yield for $A \leq 4$.

Typical differential energy spectra at $\theta_L = 30°$ and angle-integrated energy spectra are shown in Fig. 2 for ^{58}Ni. The spectra are plotted on the same scale to indicate the relative yields of the various particles. Figure 2(a) demonstrates the general forward angle behavior of the particle spectral shapes which results from the deuteron bombardment. From Fig. 2(b) one sees that the proton yield is larger than any other particle observed. This is also the case for other targets studied. The characteristic of the spectra in each region observed for medium-energy deuteron bombardment is summarized in Fig. 2(a). The most striking feature is a broad peak in the proton spectrum at about half of the incident deuteron energy. This peak will be discussed later. Another striking feature of the data is the flat spectra of high-energy deuterons, tritons, and ^{3}He at forward angles. As can be seen from Fig. 2, the cross

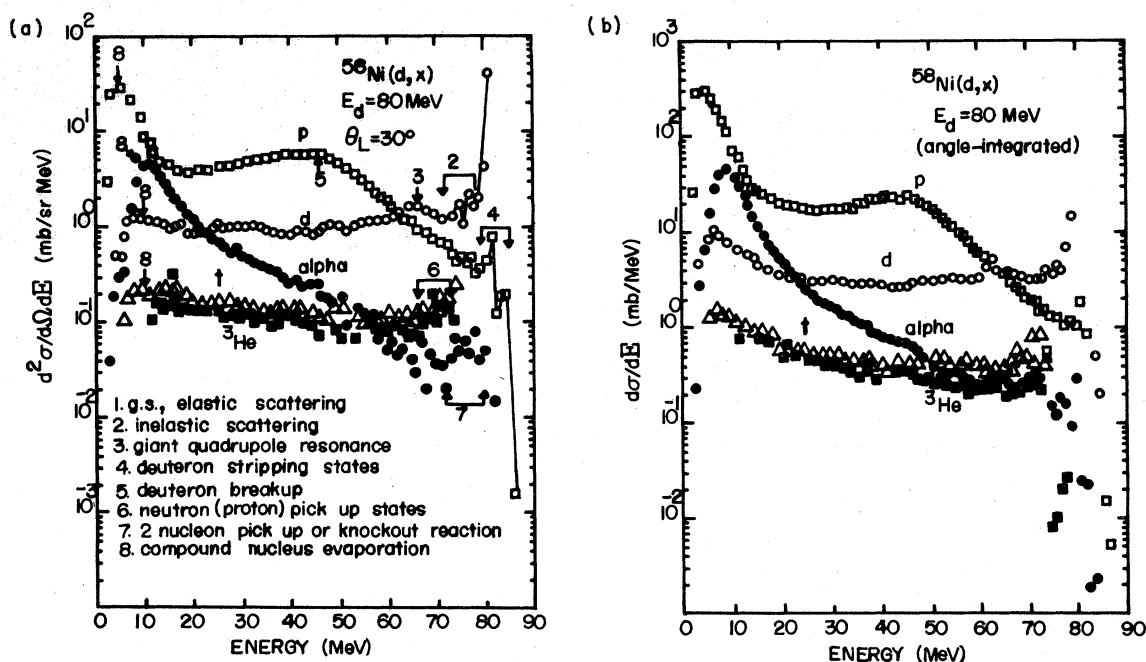FIG. 2. (a) Differential energy spectra at $\theta_L = 30°$, and (b) angle-integrated energy spectra for p, d, t, ^{3}He, and α particles from 80 MeV deutrons on ^{58}Ni.

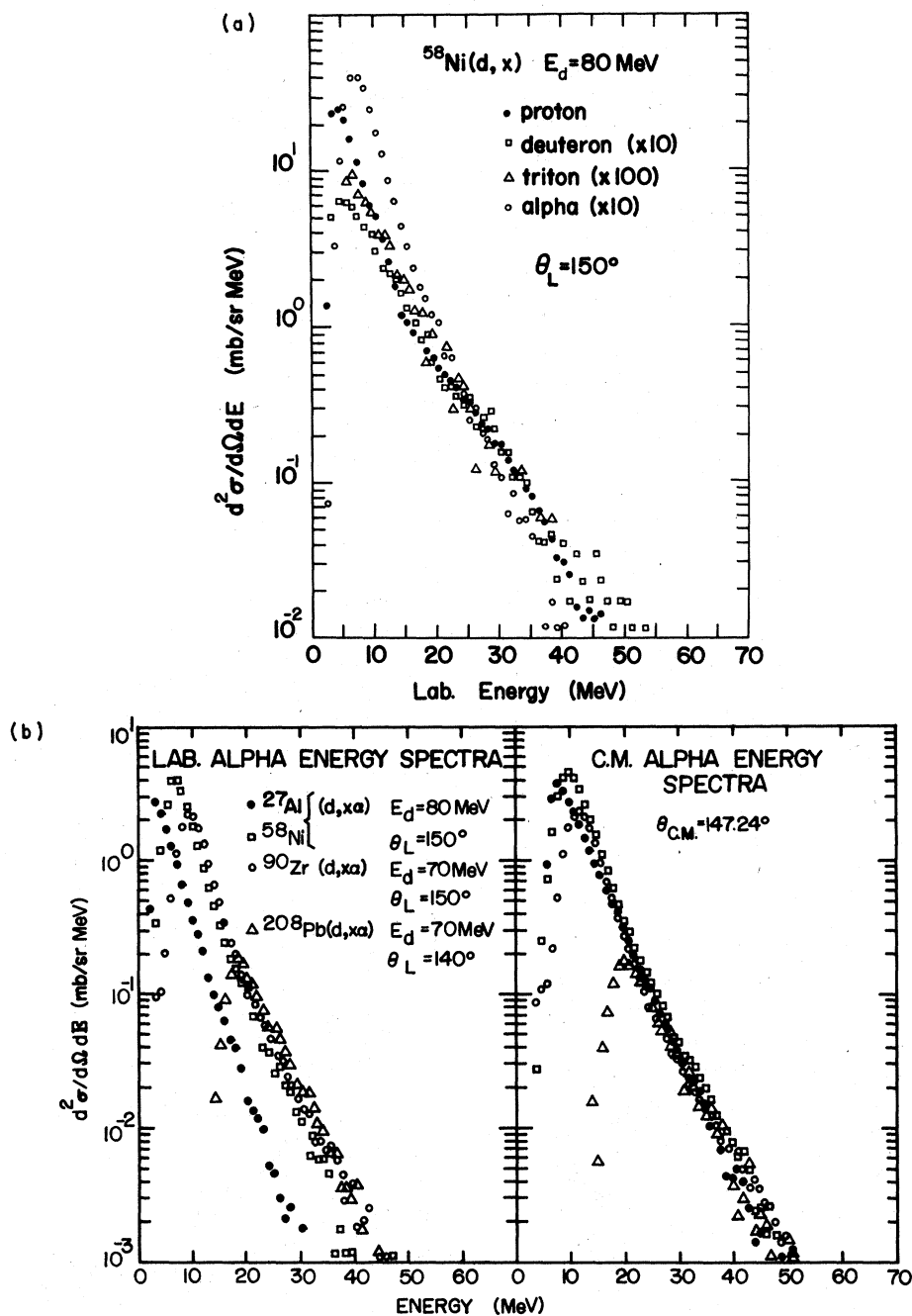FIG. 3. (a) Differential energy spectra at $\theta_L = 150°$ for p, d, t, and α particles from 80 MeV deuterons on ^{58}Ni. d, t, and α particle spectra have been multiplied by 10, 100, and 10, respectively. (b) Comparisons of α particle energy spectra at backward angle for various targets.

section leading to the discrete low-lying states, except for the elastic scattering peak, represents only a small fraction of the total reaction cross section (determined from optical model analysis of elastic-scattering data). The spectra are generally quite smooth and structureless for excitation energy above the particle-emission thresholds ex-

cept for a broad intense peak for low-energy protons and α particles.

Figure 3(a) shows the typical energy spectra obtained at backward angles for the reaction ^{58}Ni(d,x) at $E_d = 80$ MeV and $\theta_L = 150°$. The spectral shapes for $E > 20$ MeV are quite similar for all emitted particles and the magnitudes for d, t, and α par-

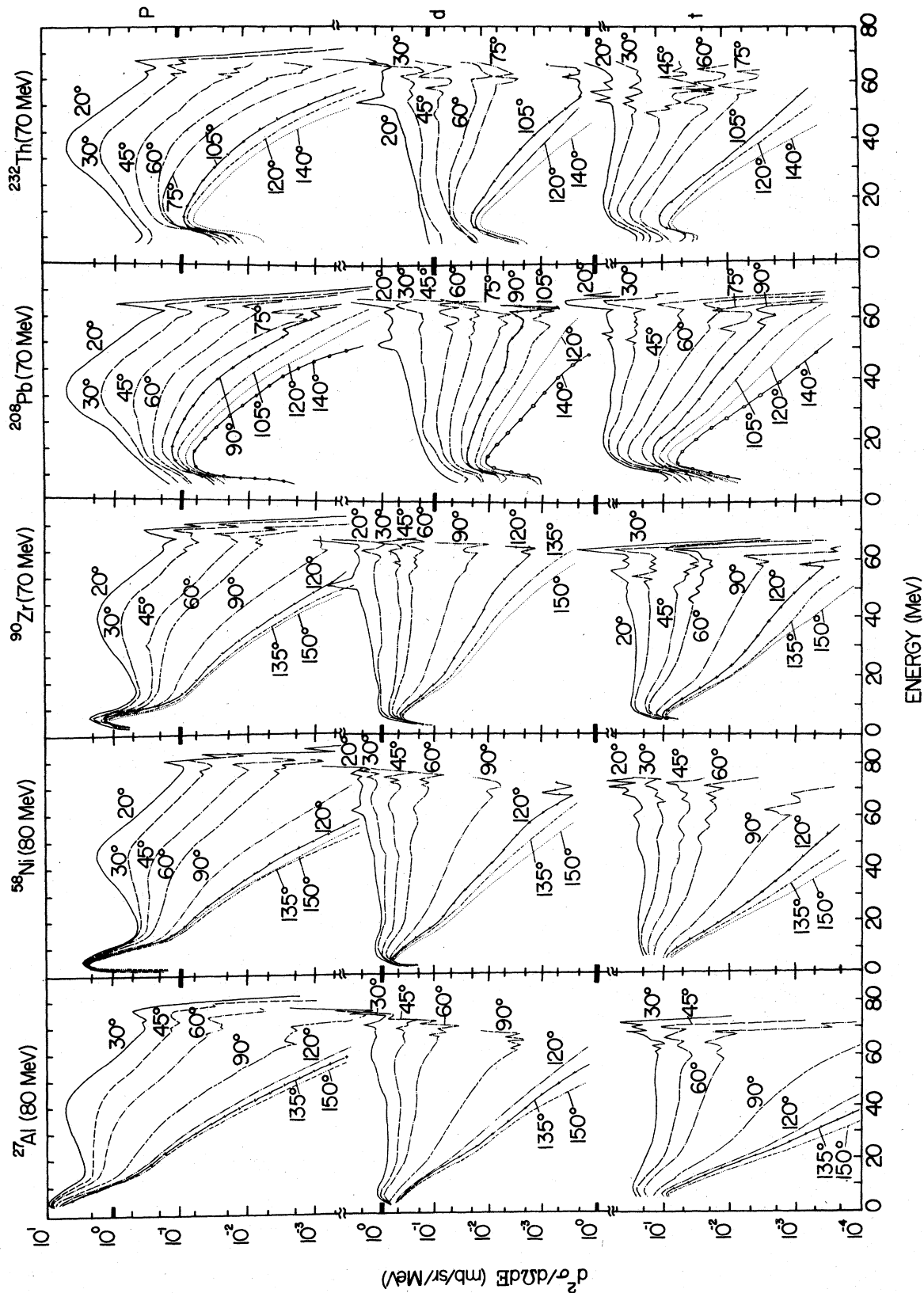FIG. 4. Differential energy spectra at angles from 20° to 150° for p, d, t, ^{3}He, and α particles from 80 MeV deuterons on ^{27}Al and ^{58}Ni, and 70 MeV deuterons on ^{90}Zr, ^{208}Pb, and ^{232}Th. The heavy mark represents the cross section of 1 mb/sr/MeV.
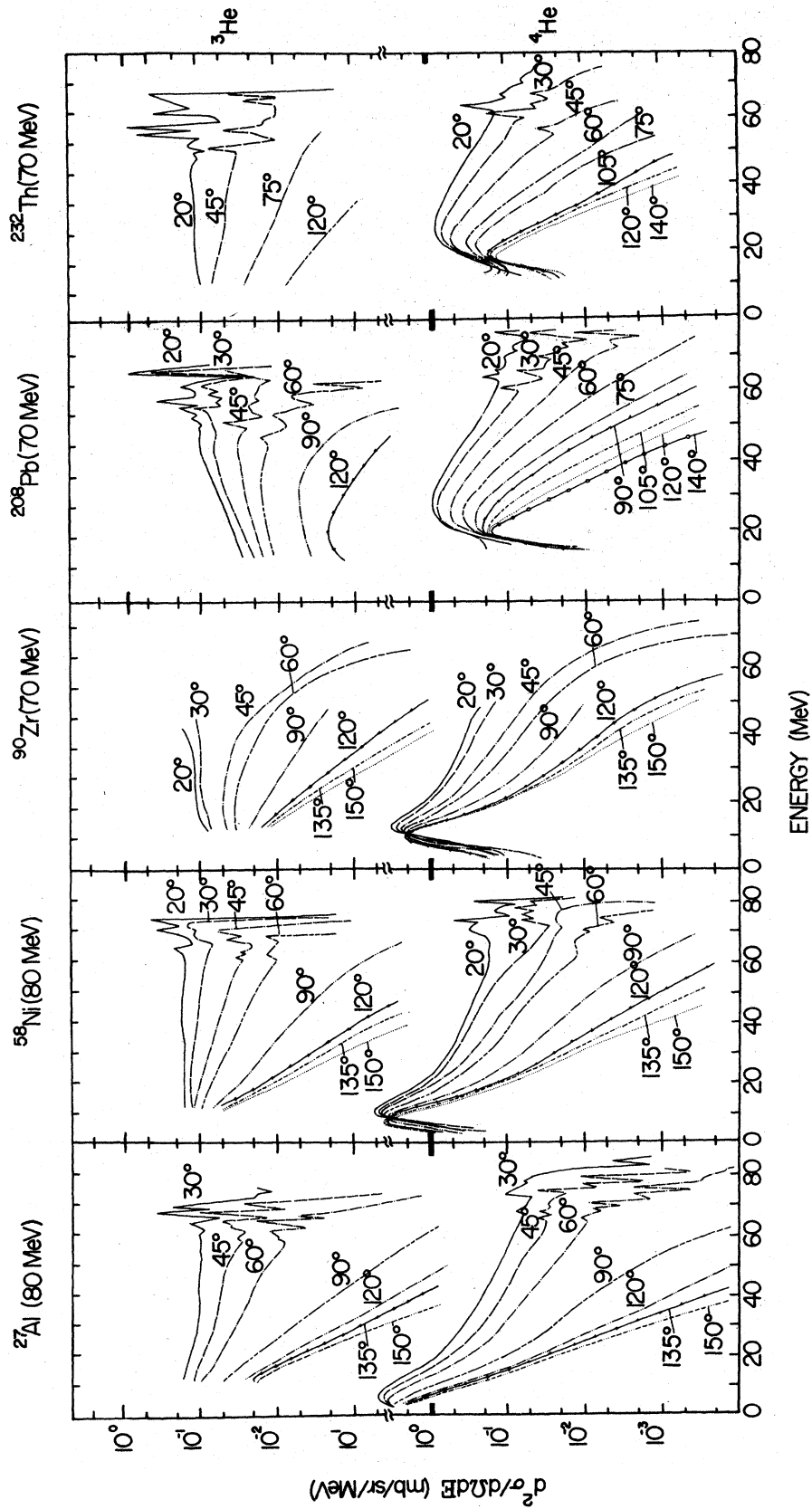
FIG. 4. (Continued)

ticles are approximately 1/10, 1/100, and 1/10, respectively, of proton yield. A similar behavior is also seen in the case of 90 MeV protons and 140 MeV α-particles induced reactions.[16] This suggests that the same process accounts for the production of particles in the backward direction for all projectiles.

Figure 3(b) shows the comparison of α-particle energy spectra obtained at backward angles for various targets. It is interesting to note that in the c.m. system, the spectral shape as well as the magnitude are similar for all targets above the low-energy peak.

Figure 4 displays the measured laboratory differential energy spectra of p, d, t, ^{3}He, and α particles for ^{27}Al, ^{58}Ni(d,x) at $E_d=80$ MeV and ^{90}Zr, ^{208}Pb, ^{232}Th(d,x) at $E_d=70$ MeV. This figure is intended only to illustrate the similarity in the

shapes and the systematic angular dependence of the spectra for the various emitted particles and target nuclei. Numerical cross sections for these spectra can be obtained from the authors upon request. As can be seen from Fig. 4, for the same type of emitted particle, a similar shape is observed for all target nuclei at a given angle, except at the very low-energy end of the spectra. Such a similarity suggests that essentially the same basic reaction mechanisms are involved in each reaction. The yields for d, t, ^{3}He, and α particles relative to protons vary from target to target. Generally, the ratios d/p and t/p increase with A, while those for ^{3}He$/p$ and α/p decrease with A.

For heavy nuclei, the triton yield is much larger than the ^{3}He yield, as one might expect because the ratio of N/Z is larger for heavy nuclei. The higher Coulomb barrier also inhibits the emission

TABLE II. Summary of the experimental results.

Target	Emitted particle	Total integral cross section σ_β (mb)	$\dfrac{\sigma_\beta}{\sigma_t}$	Mean particle yield $Y_\beta=\dfrac{\sigma_\beta}{\sigma_R}$	MeV/Reaction $=\bar{E}\times Y_B$	Discrete states cross section (mb) [a]	Evaporation cross section (mb) [b]	Non-equilibrium cross section (mb) [c]	Total mean particle yield $Y=\dfrac{\sigma_t}{\sigma_R}$
^{27}Al	p	984	0.596	1.025	20.95	4	380	600	
	d	266	0.161	0.277	13.91	35	51	180	
	t	40	0.024	0.041	1.24	6	6	28	1.719
	^{3}He	23	0.014	0.024	0.90	3	2	18	
	^{4}He	338	0.205	0.352	3.91	1	153	184	
^{58}Ni	p	2717	0.771	1.775	29.84	9	1667	1041	
	d	328	0.093	0.214	7.24	50	73	205	
	t	39	0.011	0.026	0.85	5	8	26	2.304
	^{3}He	25	0.007	0.017	0.61	2	3	20	
	^{4}He	416	0.118	0.272	3.72	1	309	106	
^{90}Zr	p	1757	0.743	0.893	17.82	17	908	832	
	d	302	0.128	0.154	5.71	56	48	198	
	t	44	0.018	0.022	0.67	7	9	28	1.202
	^{3}He	11	0.005	0.005	0.16	$\cdots$	1	9	
	^{4}He	251	0.106	0.128	1.92	$\cdots$	190	61	
^{208}Pb	p	1574	0.745	0.536	18.26	28	128	1418	
	d	377	0.178	0.128	6.30	83	18	276	
	t	80	0.038	0.027	0.92	13	9	58	0.718
	^{3}He	10	0.005	0.003	0.15	3	1	6	
	^{4}He	71	0.034	0.024	0.76	1	18	52	
^{232}Th	p	1453	0.722	0.478	16.87	19	105	1329	
	d	410	0.204	0.135	6.66	86	20	304	
	t	75	0.037	0.025	0.77	9	10	66	0.663
	^{3}He	15	0.007	0.005	0.20	2	1	12	
	^{4}He	60	0.030	0.020	0.61	1	14	45	

[a] Discrete state cross sections are estimated from 0-10 MeV in the low excitation region.
[b] Evaporation cross sections are estimated from the total cross section at 150° or 140° multiplied by 4π.
[c] Non-equilibrium cross sections are obtained by subtracting the evaporation and discrete state cross sections from the total integral cross section.

of low-energy ^{3}He particles more than tritons. The triton and ^{3}He yields are comparable for nuclei in the medium-mass region. The high-energy portions of the spectra (>20 MeV) for hydrogen particles increase with A. On the other hand, this region of the spectra for α particles is almost independent of A and decreases with A for ^{3}He.

One should notice that the total yield of protons (and α particles) is larger for ^{58}Ni than other targets studied (see also Table II). (This effect is somewhat exaggerated in our data because of the lower incident energy for the heavier targets.) Similar results were also obtained for the reactions induced by 62 MeV protons in the mass region around ^{58}Ni,[8] 90 MeV protons,[16] and 140 MeV α particles.[16]

It can be seen that the slope of the high-energy region of the spectra at low angles is much steeper for emitted α particles than for the other particles. The spectra for ^{3}He and triton have essentially the same slopes as those for deuterons. Somewhat similar behavior is also observed for proton-induced reactions.[16] In the following, the energy spectra and angular distributions for each type of particle will be discussed separately.

A. Protons

As shown on the top row of Fig. 4, the magnitude of the high-energy portion of the proton spectra decreases very rapidly with increasing angles, while the low-energy regions show little variation with angle. At the high-energy ends of the spectra (low residual excitations), pronounced discrete peaks dominate the spectra for all targets at forward angles. These discrete peaks result from deuteron stripping reactions leading to the bound states of the residual nuclei. The contribution from these states, however, is rather small in comparison with the total yield of protons.

At energies below these high-energy peaks, the spectra at low angles increase rapidly reaching a maximum at approximately a half of the deuteron incident energy. This broad peak is due to the deuteron-breakup process which dominates the yield of protons at forward angles. The deuteron-breakup yield decreases dramatically with increasing angle and the peak location shifts slightly to a lower energy. Figure 4 also shows that the breakup cross section increases with target mass.

Below the deuteron-breakup region the spectra again increase, reaching another maximum at approximately the proton Coulomb barrier energy for each target nucleus. This peak is due to the evaporation of protons. For heavy nuclei the evaporation peak at forward angles is not as pronounced as in light nuclei because the Coulomb barrier diminishes the emission of the low-energy charged

particles. (Neutron evaporation and fission are more favorable for heavier nuclei.) The evaporation peak yield decreases and peak energy shifts to higher energy with increasing mass. For angles larger than 90° the spectral shapes are similar and the magnitudes of the peak are nearly constant for a particular nucleus, indicating that the yield is dominated by the compound nuclear evaporation process. (A small nonequilibrium component also appears to exist.) This behavior allows one to estimate the total evaporation cross section. For heavy nuclei, the evaporation process amounts to less than 10 percent of the total proton yield. In addition to the dominant deuteron-breakup contribution, nonequilibrium reactions are also more important than evaporation for heavy nuclei.

For the medium-weight nuclei, the spectra show a pronounced evaporation peak with considerable high-energy cross section. The importance of the evaporation and the nonequilibrium processes is comparable.

Typical c.m. differential angular distributions for various energy bins are shown in Fig. 5 for the reaction ^{58}Ni(d,xp) at $E_d = 80$ MeV. The angular distributions behave quite smoothly and are similar for all target nuclei studied. The high-energy protons (>20 MeV) show a strong forward peaking which suggests that direct or nonequilibrium processes dominate the reaction in this region of the spectra. The distribution of the low-energy protons is nearly isotropic for lighter nuclei and is slightly forward peaked for heavy nuclei.
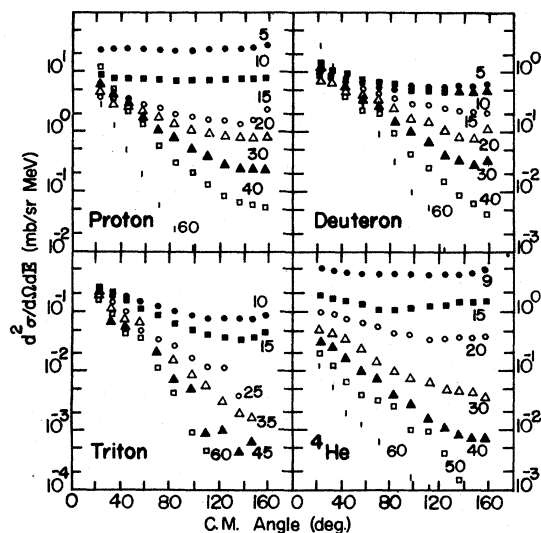

FIG. 5. Differential angular distributions for various energy bins of p, d, t, and α particles from 80 MeV deuterons on ^{58}Ni. The numbers indicated are the bin energies in MeV.

B. Deuterons

The deuteron energy spectra are shown in the second row of Fig. 4. The spectral shapes and the magnitude of the yields vary rapidly with angle. At forward angles the spectral shapes are flat or may even rise slightly at the high-energy end. For some of the nuclei, a broad peak located at $63/A^{1/3}$ of excitation energy is consistently seen at forward angles. This peak has been previously identified as the isoscalar giant quadrupole resonance (GQR).[10] Between the GQR region and the elastic peak, several discrete peaks corresponding to inelastic scattering to bound states of the residual nuclei are also seen. The yield due to the bound state region is less than 15 percent of the total deuteron yield. Most of the energetic deuterons are emitted in the forward directions, corresponding to small momentum transfers to the target nuclei. At larger angles the spectra show a rapid decrease in the deuteron yield with increasing energy. For angles larger than 90°, the similarity of the spectral shapes as well as nearly constant yield suggest that the low-energy deuterons are primarily due to evaporation. The evaporation yield of deuterons is considerably smaller than that for protons: for ^{58}Ni about 60% of the protons emitted are due to evaporation, whereas only 20% of the deuterons are due to evaporation. Figure 5 shows the typical angular distributions for various energy bins for the ^{58}Ni target.

The systematic behavior of the deuteron spectra is very similar to that observed for proton emission. The spectra of protons and deuterons differ primarily as a result of the small evaporation component of the deuteron spectra and the breakup component on the proton spectra.

C. Tritons

At forward angles, the triton energy spectra also exhibit a characteristic flat continuum. At the high-energy end, corresponding to low excitations, some discrete states are observed at low angles. Again, the yield resulting from these discrete states is less than 15% of the total yield of tritons. The angular dependence of the spectral shapes and the magnitudes with angle is very similar to that of the deuterons decreasing dramatically with angle, especially for heavy nuclei over the entire energy range (see Fig. 4). This observation implies that the evaporation of tritons is not important. The triton yield, which increases with A, is about 1/10 the yield of deutrons.

D. ^{3}He

Because of the lower yield, the ^{3}He spectra showed more statistical fluctuations than the spec-

tra of other particles. In Fig. 4, the spectra for only a few angles for ^{208}Pb and ^{232}Th are shown. Part of the ^{3}He spectra are missing from ^{90}Zr for some angles because of the failure of detecting systems during the run. The ^{3}He spectrum also exhibits a flat continuum very similar to the triton spectrum at forward angles. The high-energy region of the spectra is dominated by discrete peaks which account for of the order of 15% of the total ^{3}He yield.

The ^{3}He yields are comparable to the triton yields for ^{27}Al and ^{58}Ni but are much less for heavier target nuclei. The great similarity in spectral shapes and magnitudes between ^{3}He and triton for ^{27}Al and ^{58}Ni implies that there is nearly an equal chance for a deuteron to pick up either a proton or a neutron in this mass region. The energy spectra also show that the evaporation mechanism is unimportant.

E. α particles

As shown in Fig. 4, the structure of the α particle spectra at high energies is ambiguous because of the poor statistics. Note that the failure of the detector system during the ^{90}Zr run also resulted in the loss of some α-particle data for this target. The yield of high-energy α particles is a factor of 2 or 3 times smaller than the high-energy yield of tritons and ^{3}He. The spectral shapes for α particles are quite similar at energies higher than ~20 MeV for all nuclei investigated. The energy spectra increase smoothly in magnitude with decreasing energies until a broad maximum is reached at approximately the energy of the Coulomb barrier and then fall off rapidly. The high Coulomb barrier clearly prohibits the emission of low-energy α particles for heavy nuclei.

The yield of high-energy α particles decreases rapidly with increasing angle. At the same laboratory angles, the high-energy yield of α particles is surprisingly large when compared to the same regions of the triton and ^{3}He spectra. One would expect two-nucleon pickup or α-particle knockout to be much less important than single-nucleon pickup or stripping. The low-energy yield of α particles is approximately independent of angle for the lighter nuclei. Clearly, the α-evaporation process plays an important role for α-particle emission in the light- and medium-mass nuclei.

All of the evaporation peaks shown in Fig. 4 shift to lower energies as the angle increases. Such a shift in energy suggests that the evaporating particles are emitted from a recoiling nucleus. The momentum of the recoiling nucleus deduced from the shift corresponds to almost the entire momentum of the incident projectile. The variation of α peak energy with laboratory angles
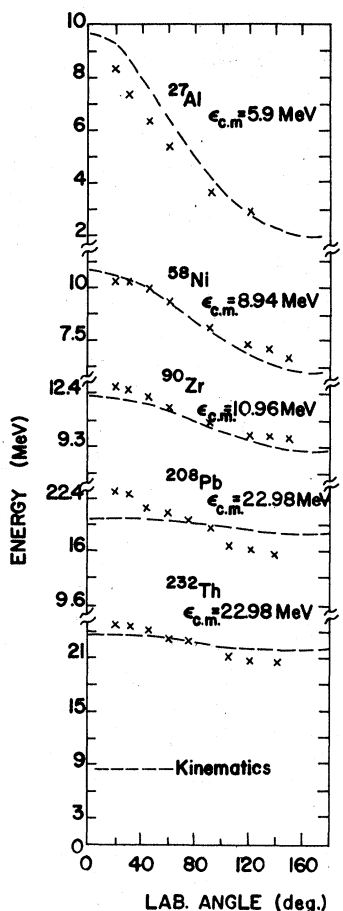
FIG. 6. The variations of α-particle evaporation peak energy with laboratory angles and comparisons with two-body kinematics for various target nuclei.

FIG. 7. The c.m. energy spectra of α particles at several c.m. angles for 80 MeV deuterons on ^{58}Ni.

is shown in Fig. 6 for all targets studied. The dashed curves represent two-body kinematics assuming only one emitted particle. The corresponding c.m. energies of α particles are also indicated. For light- and medium-weight nuclei, the observed evaporation peak locations follow the two-body kinematics rather well. To confirm this kinematic shift, we have plotted in Fig. 7 the c.m. energy spectra transformed from the laboratory spectra according to Eq. (1) at several c.m. angles for the ^{58}Ni($d,x\alpha$) reaction. It can be seen that all spectra are peaked at the same location in the c.m. frame. As discussed previously, the evaporation of charged particles is considerably less important for heavy target nuclei. The pre-equilibrium emission tends to obscure the evaporation peak at forward angles and makes the location of the peak very uncertain. This could account for the apparent anomalous shift in the peak indicated for the heavy nuclei.

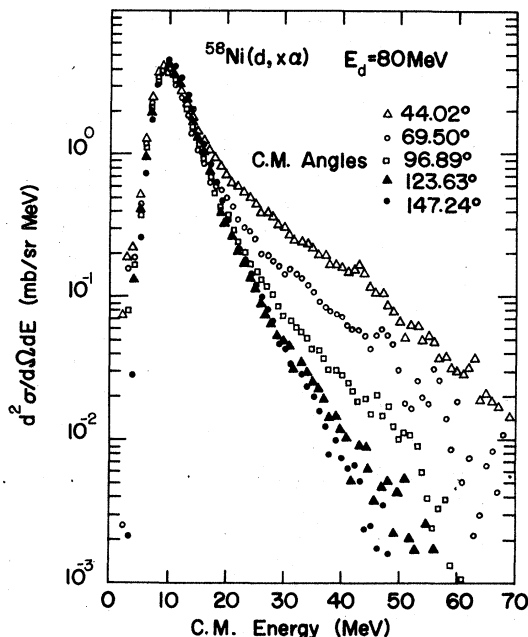A brief summary of experimental results is pre-

sented in Table II. The important features observed for the medium-energy deuteron-induced reactions are outlined below:

(1) The deuteron-breakup process dominates the proton spectra at forward angles. The breakup yield increases with increasing target mass A.

(2) For all target studied, the high-energy continuum of all emitted particles decreases rapidly in magnitude with increasing angle (strongly forward peaked). For the lighter nuclei, the low-energy region is dominated by an evaporation peak which is nearly isotropic in the c.m. A small nonequilibrium yield is also observed at backward angles in many reactions. The energy spectra are rather constant at backward angles ($> 90°$).

(3) The highest-energy particles are produced via direct reactions leading to the bound states of residual nuclei. These low-lying states (integrated up to 10 MeV excitation energy) represent only a few percent (6%) of the total integral charged light-particle yield (see Table II).

(4) The evaporation process (~50% of total charged light-particle yield) is comparable to the nonequilibrium process in light- and medium-mass nuclei, while the nonequilibrium (over 90% of the total charged light-particle yield) processes dominate the emissions of charged particles for heavy nuclei.

(5) Except for the deuteron-breakup peak in the proton spectra, the high-energy portion of the spectra of all other particles are relatively flat at small angles. This flatness and the rapid angular depen-
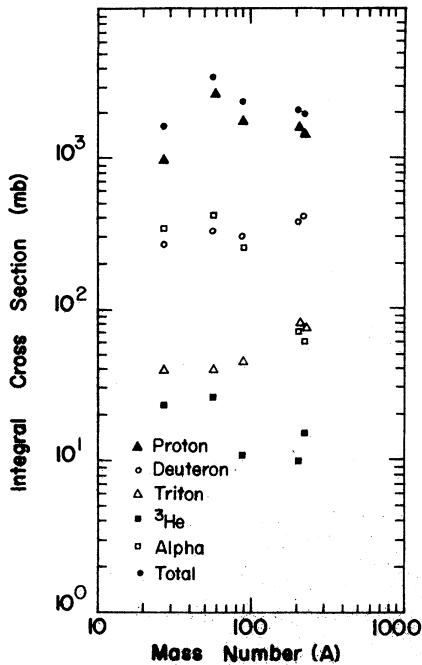
FIG. 8. The variation of total production cross section for various charged light particles ($Z \leq 2$, $A \leq 4$), and the total charged light-particle yield with target nuclear mass.
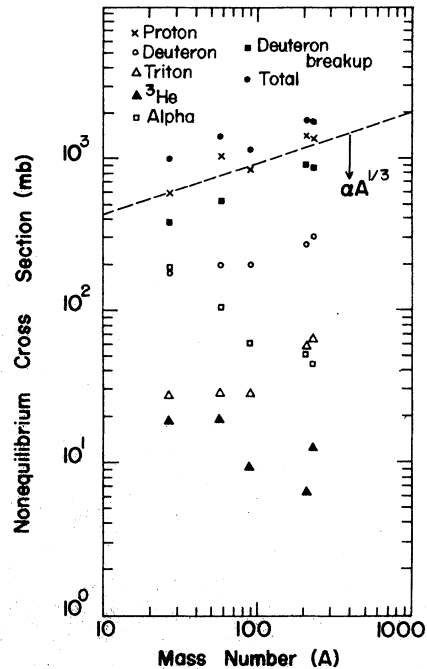

FIG. 9. The variation of nonequilibrium charged light-particles cross sections, and the total nonequilibrium charged light-particle yield with the target nuclear mass. The straight line shows the $A^{1/3}$ dependence.

dence of the high-energy particles suggest that direct or semidirect processes involving relatively few interactions dominate this region of the spectra.

(6) The total yield of charged light particles σ_t plotted as function of A in Fig. 8 appears to reach a maximum in the region around ^{58}Ni. The decrease in charged light-particles yield for heavy mass nuclei undoubtedly reflects the increasing importance of neutron emission and fission, as the increasing Coulomb barrier inhibits the emission of low-energy charged light-particles. Note that the total production of deuterons and tritons continues to increase with A because evaporation plays only a very small role in the production of these particles.

(7) The spectral shapes of a given particle type above the evaporation peak are similar for all target nuclei studied (see Fig. 4). Figure 9 shows a log-log plot of the nonequilibrium yields of various charged light-particles σ'_β and the total nonequilibrium charged light-particle yield σ'_t (nonequilibrium yield which is obtained by subtracting the most backward angle energy-integrated cross section multiplied by 4π from total integral cross section) vs A. $\sigma'_t/A^{1/3}$ has a rather constant value $\sigma'_t \sim (300 \pm 50)A^{1/3}$mb. The production of energetic (nonequilibrium) protons and deuterons appears to be proportional to the nuclear radius, suggesting

that these particles may result from the peripheral collisions. Tritons, ^{3}He, and α may involve a more complicated process.

(8) The total proton yield (see Table II) is found to be ~60–80 % of the total charge light-particle yield.

IV. COMPARISON WITH CALCULATIONS

The compound-nucleus evaporation mechanism seems adequate in describing the low-energy region of the spectra for the lighter nuclei. However, the model fails to account for the observed spectra above 20 MeV. The compound-nucleus evaporation is the last stage of a nuclear equilibration process. The failure of this model to predict sufficient yields of the high-energy particles suggests that a reaction mechanism bridging the energy region between the direct interaction to bound states and the compound-nuclear evaporation is needed. Several models of such mechanisms have been developed in recent years, such as the direct reaction, the quasifree scattering, the intranuclear cascade (INC),[2] and the pre-equilibrium model.[4] Some of these models seem to be reasonably successful in accounting for the gross features of the experimental data. In this paper, we have analyzed the data within the framework of the pre-equilibrium exciton model together with evaporation theory.[17,18] This

model has a serious limitation in that it can only be compared with the experimental angle-integrated energy spectra. Nevertheless, it provides a qualitative guide which suggests that much of the high-energy component of the spectra results from relatively simple interactions of the projectile with the target nucleus. In the case of protons produced via deuteron breakup, we have compared the results with the prediction of a simple deuteron-breakup model originally developed by Serber.[14]

A. Pre-equilibrium exciton model and evaporation model calculations

At angles beyond 90°, where direct reactions are expected to be relatively unimportant, many of the spectra exhibit the characteristics of the evaporation process. Comparisons are made between the c.m. spectra at backward angles and the pure evaporation calculations (normalized to data) in Fig. 10. The level density parameter $a = g\pi^2/6$, where g is single-particle level density, is taken to be $A/8$, i.e., $g = 3A/4\pi^2$ MeV^{-1}, for all calculations carried out in this paper. The evaporation calculation fails to predict the shape of spectra for energies greater than 20 MeV even at such large angle.

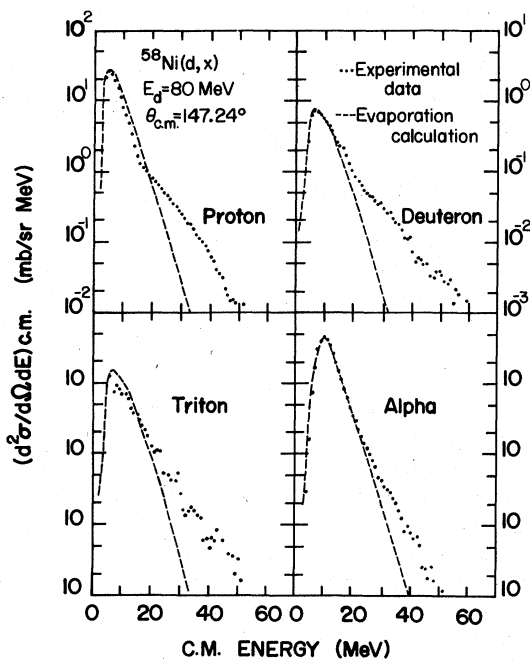The pre-equilibrium exciton model assumes that the composite system equilibrates from the initial particle-hole state ($p_0 + h_0$) formed by a two-body interaction between a nucleon in the projectile with a nucleon in the target. The system is then assumed to proceed to more complex particle-hole states through a series of two-body collisions. Particles may be ejected after the first few collisions with rather high energies. Details of the pre-equilibrium exciton model used to analyze these data are given in Refs. 17 and 18. All symbols used in this paper are the same as those of Refs. 17 and 18.

Pre-equilibrium calculations indicate that the high-energy particles result primarily from the lowest particle-hole state ($p + h$) from which the particle type β can be emitted. From Eq. (5) of Ref. 17 we see that to first order the high-energy
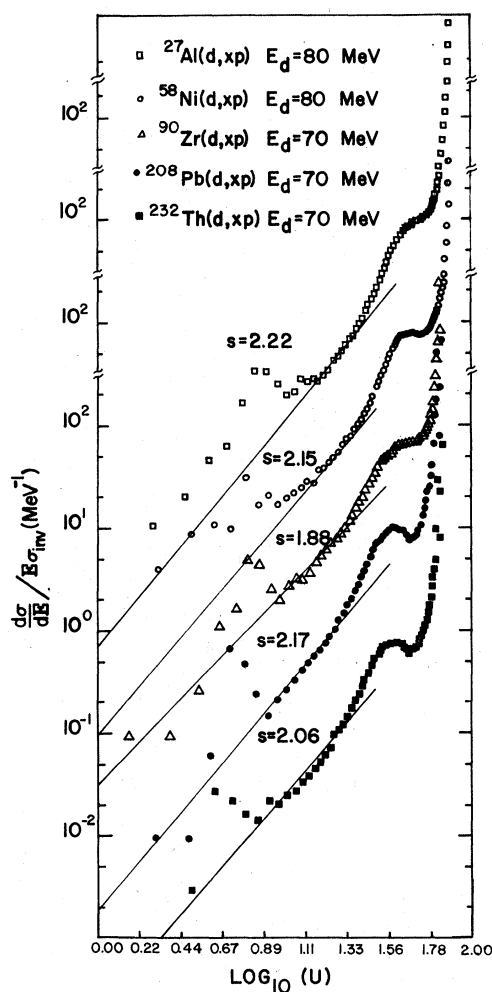

FIG. 10 The comparison of experimental particle energy spectra at $\theta_{c.m.} = 147.24°$ with the evaporation calculations for 80 MeV deuterons on ^{58}Ni. Evaporation calculation with a level density parameter $a = A/8$ have been normalized to the experimental data.

FIG. 11 Plot of $\left(\frac{d\sigma}{d\epsilon}\right)_{c.m.}/\epsilon\,\sigma_{inv}(\epsilon)$ vs U (excitation energy) for protons resulting from deuteron-induced reactions for various target nuclei. The slopes are indicated in each spectrum. This slope analysis yields a value of 2 for s which suggests an initial $3p$-$1h$ configuration.

portion of the spectrum is given by

$$\frac{d\sigma_\beta(\epsilon)}{d\epsilon} \propto \epsilon\sigma_\beta(\epsilon)U^{p+h-\beta-1} , \qquad (2)$$

where $\sigma_\beta(\epsilon)$ is the inverse reaction cross section for particle β at energy ϵ, and U is the excitation energy of the residual nucleus. The proportionali-

ty constant contains all other information required in the exciton model. From the above equation one finds that the slope of

$$\log\left[\frac{d\sigma_\beta(\epsilon)}{d\epsilon}\Big/\epsilon\sigma_\beta(\epsilon)\right] \text{ vs } \log(U)$$
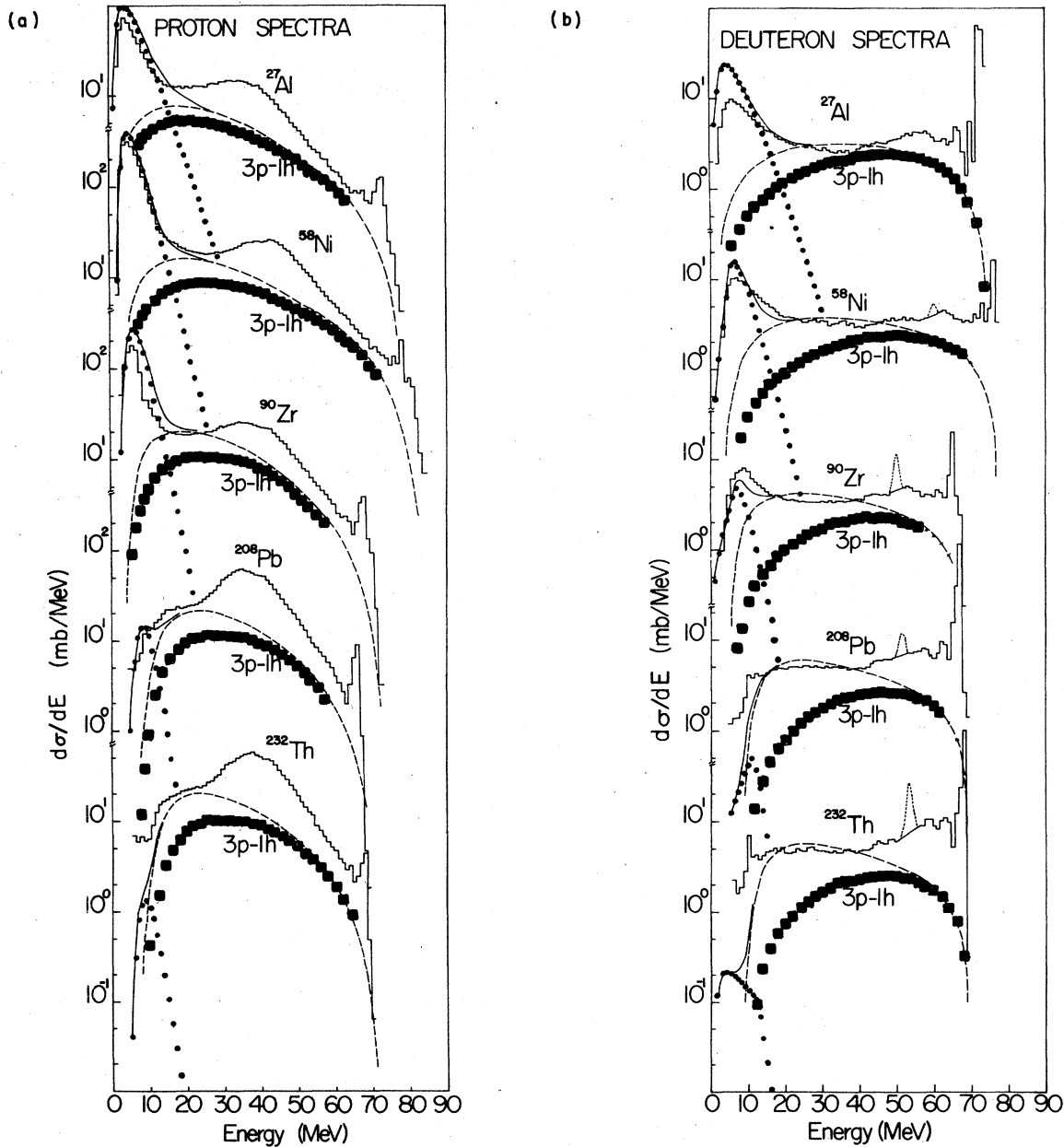
is related to p and h by

FIG. 12. (a) The comparisons of experimental proton angle-integrated energy spectra with pre-equilibrium exciton model plus evaporation model calculations. ⌁⌁ represents the experimental data; ■■■ represents the calculated pre-equilibrium spectra from the first stage as indicated; --- represents the calculated total pre-equilibrium spectra; ●●● represents the calculated evaporation spectra; and —represents the sum of calculated total pre-equilibrium and evaporation spectra. (b) Same as (a) except for deuteron. (c) Same as (a) except for triton. (d) Same as (a) except for ³He. (e) Same as (a) except for α particles.

$$p + h = s + \beta + 1. \tag{3}$$

Hence, the analysis of the slope of the experimental data can often provide an estimate of the first particle-hole configuration from which particle β can be emitted. The results of such analyses are presented in Fig. 11 for protons.

The most probable value of the initial exciton number deduced from these analyses is found to be 4; i.e., 3p − 1h. In the case of α-particle emis-

sion p + h is found to be 6; i.e., 4p − 2h. As the model assumes that the incident projectile interacts with the target nucleus by exciting one of the target nucleons to form a certain initial particle-hole configuration, a 3p − 1h initial state for deuteron-induced reaction is expected. An α particle cannot be emitted from the 3p − 1h state, hence the first particle-hole state from which α-particle emission is possible is the 4p − 2h state. This is also in agreement with the slope analysis.
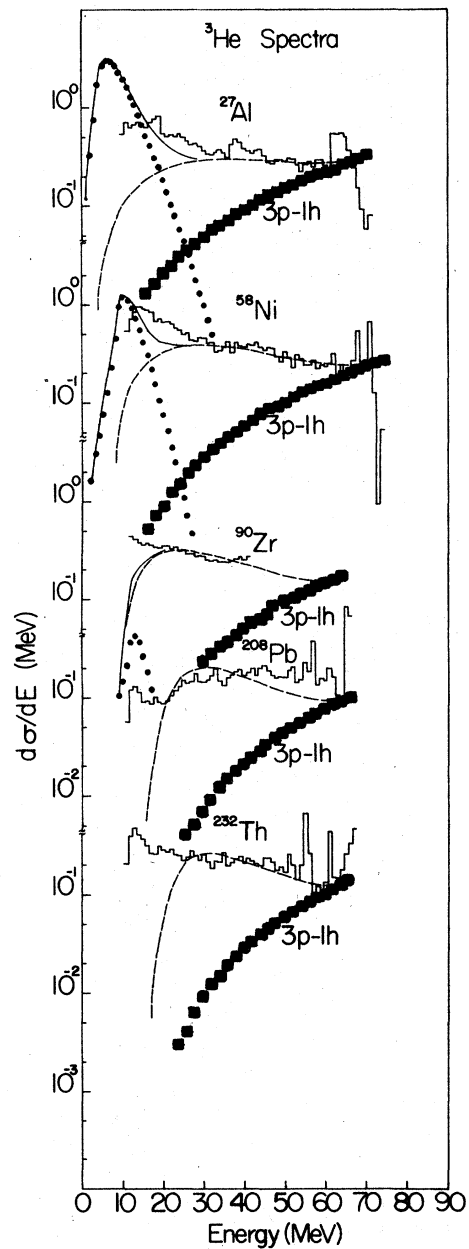
(c)
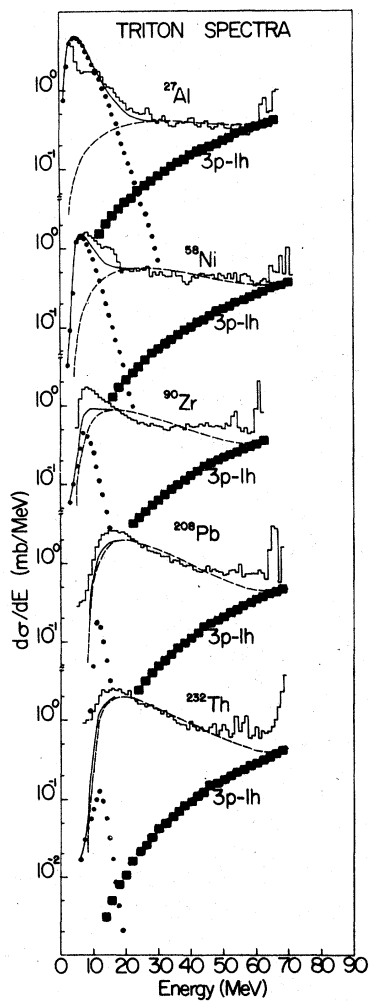
(d)

Fig. 12. (Continued)

Figures 12(a)–12(e) show comparisons be-
tween the calculations and the experimental angle
integrated spectra in the c.m. frame. The calcu-
lation consists of three parts: (1) the pre-equili-
brium component shown as dashed curves; (2)
evaporation following the pre-equilibrium emis-
sions; (3) pure evaporation [evaporation which re-
sults from the equilibrating system proceeding to
equilibrium without the emission of particles in the
earlier stages as defined in Eq. (17) of Ref. 17.]
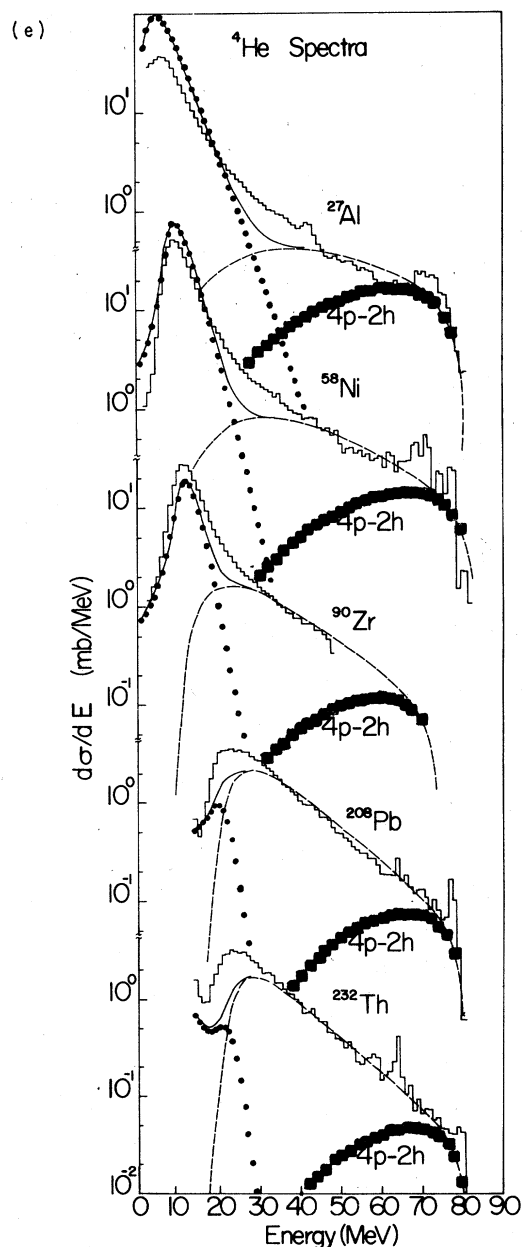The contributions from (2) and (3) combined are

Fig. 12. (Continued)

shown as dotted curves. The solid curves are the
sums of all three components.

The following parameters are used in the pre-
equilibrium calculations:

(1) The averaged two-body transition matrix ele-
ments used in the present calculations are given by
$|M|^2 = KA^{-3}E^{-1}$.[19] A value of $K = 200$ MeV^3 was found
to give reasonable agreement between the calcula-
tions and the experimental data for all targets
studied.

(2) The inverse reaction cross sections $\sigma_\beta(\epsilon)$ for
the pre-equilibrium calculations are calculated
from an optical model analysis using a global set
of parameters taken from Refs. 20 and 21. In the
evaporation calculations, empirical expressions
which reproduce the inverse reaction cross sec-
tions calculated from the optical model are used.[15,22]

(3) The total reaction cross section $\sigma_R(E)$ is
needed in the calculation of the absolute cross sec-
tions. Since no experimental $\sigma_R(E)$ were available
for 70 or 80 MeV deuterons, they were computed
from the optical model with parameters obtained
from Refs. 15 and 23. These values of $\sigma_R(E)$ are
listed in Table III.

A comparison between the experimental data and
the calculations leads to the following observations:

(1) The pre-equilibrium exciton model predicts
a rather large cross section in the region of high-
energy continuum of the spectra. In heavy nuclei,
the pre-equilibrium reactions dominate the entire
energy spectrum of charged light particles.

(2) The pre-equilibrium calculations agree well
with the high-energy components of the angle-inte-
grated energy spectra both in shape and in absolute
magnitude. The calculated pre-equilibrium proton
spectrum provides a reasonable continuum under-
lying the deuteron-breakup peak.

(3) As shown in Figs. 12(a)–12(e), the spectra
resulting from the 3p – 1h states for p, d, t, and
^{3}He and the 4p – 2h states for α particles account
for most of the highest-energy charged light par-
ticles emitted. The results also show that the con-
tributions from states formed after a few collisions
(from higher exciton states) are important, partic-
ularly for t, ^{3}He, and α particles. In the case of
deuterons, the pre-equilibrium calculations do not
predict enough yield for high-energy particles.
This is expected because the pre-equilibrium mod-
el does not include any effect of collective excita-
tion which is dominant in the high-energy region of
the inelastic spectrum.

(4) Deuterons emitted from 3p – 1h states are
equivalent to inelastic scattering, which leads to
1p – 1h excited states in the residual nucleus. The
emission of tritons (or ^{3}He) from the 3p – 1h state
corresponds to the pickup of a neutron (or a pro-
ton) by the incident deuteron, leading to 1 neutron-
hole (or 1 proton-hole) states in the residual nu-

TABLE III. Summary of the calculated results.

Target	Total reaction cross section (mb) σ_R	Initial particle and hole number	Emitted particle	Measured non-equilibrium cross section	Complex particle formation probability — No pairing correction	Complex particle formation probability — pairing correction	Calculated pre-equilibrium cross section — total (mb)	Calculated pre-equilibrium cross section — first stage (mb)	Estimated deuteron breakup cross section (mb) [a]
^{27}Al	959.4	3p-1h	p	600	•••	•••	293	217	
		•	d	180	0.0315	0.0312	155	105	307 (80 MeV)
			t	28	0.00772	0.00686	22	10	
			^{3}He	19	0.00668	0.00739	19	8	
			^{4}He	184	0.0169	0.0175	18	5	
^{58}Ni	1531.0	3p-1h	p	1041	•••	•••	619	382	
			d	205	0.0203	0.0218	183	101	422 (80 MeV)
			t	26	0.00432	0.00421	29	8	
			^{3}He	20	0.00332	0.00332	20	6	
			^{4}He	106	0.00748	0.00645	29	4	
^{90}Zr	1967.2	3p-1h	p	832	•••	•••	537	262	
			d	198	0.0161	0.0177	175	85	295 (70 MeV)
			t	28	0.00305	0.00312	31	8	
			^{3}He	9	0.00178	0.00176	12	3	
			^{4}He	61	0.00478	0.00369	45	4	
^{208}Pb	2934.7	3p-1h	p	1418	•••	•••	663	390	
			d	276	0.0163	0.0175	230	97	755 (70 MeV)
			t	58	0.00257	0.00269	64	9	
			^{3}He	6	0.00103	0.00102	7	2	
			^{4}He	52	0.00207	0.00190	44	2	
^{232}Th	3037.6	3p-1h	p	1329	•••	•••	619	363	
			d	304	0.0167	0.0181	215	93	710 (70 MeV)
			t	66	0.00229	0.00236	62	8	
			^{3}He	12	0.00152	0.00153	9	2	
			^{4}He	45	0.00144	0.00130	35	1	

[a] Deuteron breakup cross section is estimated by subtracting calculated pre-equilibrium cross section from measured non-equilibrium cross section of proton.

cleus. Similarly, the two-nucleon (1 proton and 1 neutron) pickup process corresponds to an α particle being emitted from 4p − 2h states. The pre-equilibrium calculations suggest that these simple one- and two-nucleon pickup processes only account for a small fraction of the non-equilibrium yield of t, ^{3}He, and α particles. More complex interactions, such as multiple scattering, are important in the production of such particles.

The direct-stripping process leading to the excitation of 1 neutron particle states in the proton spectrum is not included in these pre-equilibrium calculations, unless an initial 2p − 0h state is assumed. This stripping process would be expected to include the deuteron-breakup contribution. The calculation, using a 2p − 0h state, however, predicts a flat spectral shape for protons, in contrast to the strong peak observed in the experimental data.

(5) In the present calculations multi-particle emission in the pre-equilibrium stage is not included. The inclusion of such processes would probably reduce the yield in the evaporation regions and enhance the yield in the middle of the spectrum. This may provide better agreement between theory and data. For example, if a deuteron is emitted from a 3p − 1h state, the residual nucleus is left in excited 1p − 1h states. Particles emitted from such states may carry off relatively large amount of energy. In the present calculations these secondary pre-equilibrium emissions are treated as evaporation process for simplicity.

(6) The complex-particle formation probability γ_β extracted from these data (see Table III and Fig. 13) shows a strong dependence on A. The procedure for obtaining γ_β from the experimental data was discussed in great detail in Ref. 18. In Fig. 13 we have plotted $\gamma_\beta g/g_\beta$ instead of γ_β, where g and g_β
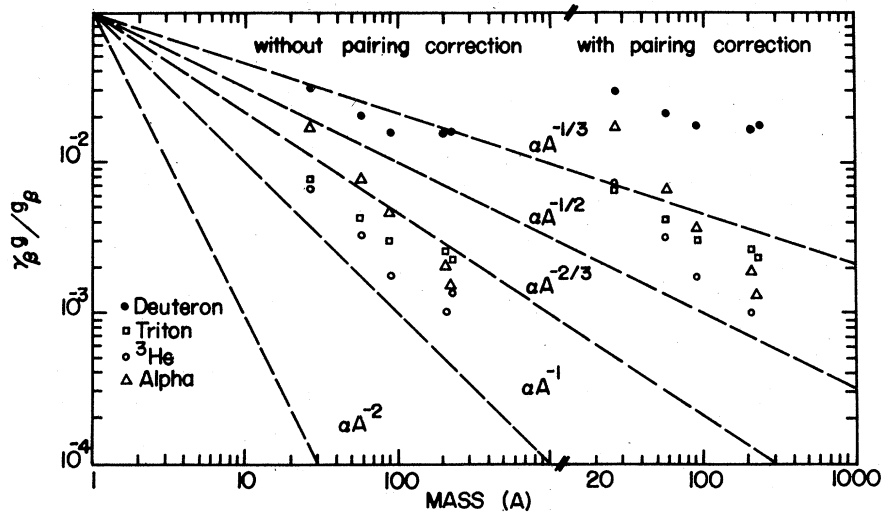
FIG. 13. Plot of $\gamma_\beta g/g_\beta$ as a function of nuclear mass t, ^{3}He, and α particle. A family of curves showing various A dependence are also plotted as dashed lines.

are single nucleon and complex-particle state densities. The γ_β's are extracted from experimental data both with and without pairing correction in the pre-equilibrium calculations.

B. Deuteron-breakup model calculations

As shown in Fig. 4, deuteron-induced reactions are dominated by the deuteron-breakup process at forward angles. The deuteron-breakup cross section increases with increasing A. It is difficult to extract the deuteron-breakup yield from the underlying continuum at a given angle. In the case of the angle-integrated spectra we have assumed that we can use the pre-equilibrium calculations to estimate the underlying continuum of protons. Figure 14 shows the angle-integrated spectra obtained by subtracting the pre-equilibrium calculations from the observed spectra. The resultant spectra shown as smooth curves are compared with the prediction of the Serber model for deuteron breakup,[14] shown as dashed curves in Fig. 14. By normalizing the calculations to the experimental cross sections, a qualitative agreement of the spectral shapes is obtained, except that the calculated peak location is shifted slightly to lower energies. In fact, the observed deuteron-breakup cross section is much larger (~2 to 4 times larger) than the predictions of Serber's model. This discrepancy is not due to the assumed background from the pre-equilibrium calculations. The total breakup cross section in the breakup model is given by $\sigma_s = \frac{1}{2}\pi R R_d$, where $R = r_0 A^{1/3}$ is the nuclear radius and R_d is the deuteron radius.[14] The model predicts the $A^{1/3}$ dependence of the breakup yield. In Fig. 9, the observed deuteron-breakup yield estimated using the pro-

cedure described above shows an approximate $A^{1/3}$ dependence.

V. CONCLUSIONS

The spectra of charged light particles produced by deuteron bombardment of five target nuclei show surprisingly systematic behavior and considerable similarity. The spectra exhibit three distinct regions: the discrete states at low-excitation energy resulting from two-body reactions, the evaporation peak, and a large continuum between
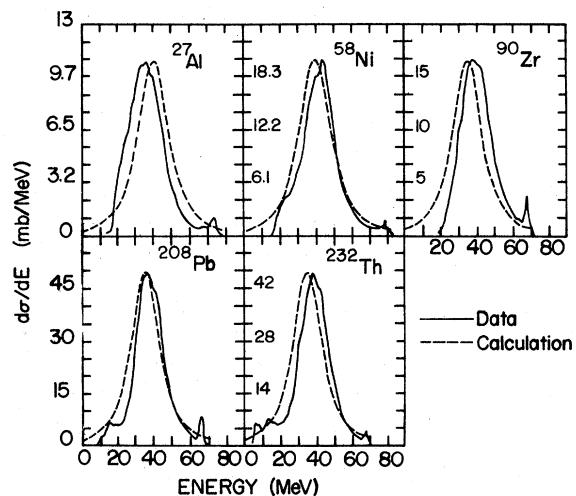

FIG. 14. Comparisons of proton enegy spectra calculated using Serber's deuteron-breakup model (dashed curves) with experimental data (solid curves). Calculation has been normalized to the experimental peak cross section.

the evaporation peak and the low-lying discrete bound states. In the angular region studied, the total yield due to the discrete states (up to about 10 MeV excitation energy) is less than 6% of the total charged light-particle yield. The extremely flat shape of the high-energy continuum region at low angle for emitted deuterons, tritons, and ^{3}He is perhaps the most striking feature of the data. The spectral shapes at all angles are also quite similar for deuterons, tritons, and ^{3}He. The nonequilibrium continuum is strongly forward peaked for all particles. The proton continuum is dominated by deuteron breakup.

Approximately 75% of the total charged light-particle yield is due to protons (except for ^{27}Al). The nonequilibrium yield of charged light particles increases with target mass and is roughly proportional to $A^{1/3}$. For lighter nuclei, approximately half of the total production cross sections are due to evaporation process. For heavy nuclei, evaporation accounts for less than 10% of the total cross section. The observed total charged light-particles yield is approximately a factor of 2 larger than the total reaction cross section except for heavy nuclei where neutron and fission competitions dominate. Clearly, multiparticle emission is important.

The pre-equilibrium exciton, the evaporation and the Serber deuteron-breakup models provide reasonable fits to the angle-integrated spectra, except in the region of the discrete states. The results show that the particles emitted with energies higher than ~20 MeV for light- and medium-weight nuclei are mostly from pre-equilibrium emission. For heavy nuclei, almost all of the charged light-particle production results from pre-equilibrium emission.

These models have the severe limitation in that they cannot provide an explanation of the dramatic angular dependence of the nonequilibrium yield. The fact that the first few particle-hole states of the pre-equilibrium model appear to account for most of the high-energy continuum and that the life times of these particle-hole states are comparable to nuclear transit times suggests that the basic mechanisms which produce the nonequilibrium yield involve the interaction of relatively few nucleons of the target with the projectile.

The overall behavior of the differential energy spectra suggests that the nuclear reaction is dominated by two types of mechanisms:

(1) One which occurs on a fast time scale, retaining the initial dynamic information where a relative simple process, such as quasi-free scattering, pickup, breakup, etc., which involves large momentum transfer interaction with relatively few target nucleons.

(2) The other which results in equilibration processes and corresponds to almost complete transfer of the incident projectile momentum to the equilibrium system.

ACKNOWLEDGMENTS

[1]P. G. Roos and N. S. Wall, Phys. Rev. 140, B1237 (1965); N. S. Wall and P. G. Roos ibid. 150, 811 (1966).

[2]M. L. Goldberger, Phys. Rev. 74, 1289 (1948); N. Metropolis et al., ibid. 110, 185 (1958); 110, 204 (1958); H. W. Bertini, ibid. 131, 1801 (1963); K. Chen et al., Phys. Rev. C 4, 2234 (1971).

[3]A. Mignerey et al., Nucl. Phys. A273, 125 (1976).

[4]J. J. Griffin, Phys. Rev. Lett. 17, 478 (1966); Phys. Lett. 24B, 15 (1967); M. Blann, Phys. Rev. Lett. 21, 1357 (1968); Annu. Rev. Nucl. Sci. 25, 123 (1975); C. K. Cline, Nucl. Phys. A172, 225 (1971).

[5]M. Blann, Phys. Rev. Lett. 27, 337 (1971); 28, 757 (1972); Nucl. Phys. A186, 245 (1972).

[6]C. C. Chang, N. S. Wall, and Z. Fraenkel, Phys. Rev. Lett. 33, 1493 (1974); R. E. Segel et al., Phys. Rev. C 13, 1566 (1976); P. P. Singh et al., ibid. 14, 1655 (1976).

[7]R. W. West, Phys. Rev. 141, 1033 (1966); V. V. Verbinski and W. R. Burris, ibid. 177, 1671 (1969); S. M.

Grimes et al., Phys. Rev. C 5, 830 (1972); A. Chevarier et al., ibid. 8, 2155 (1973); F. E. Bertrand, R. W. Peele, and C. Kalbach-Cline, ibid. 10, 1028 (1974); A. Chevarier et al., ibid. 11, 886 (1975); Nucl. Phys. A231, 64 (1974); M. Blann et al., ibid. A257, 15 (1976); L. Glowacka et al., ibid. A262, 205 (1976).

[8]F. E. Bertrand and R. W. Peele, Phys. Rev. C 8, 1045 (1973); ORNL Reports Nos.: ORNL–4450, 1969 (unpublished); ORNL–4455, 1967 (unpublished); ORNL–4460, 1969 (unpublished); ORNL–4469, 1970 (unpublished); ORNL–4471, 1970 (unpublished); ORNL–4638, 1971 (unpublished); ORNL–4799, 1973 (unpublished).

[9]J. P. Craig, Ph.D. Thesis, University of Maryland 1975 (unpublished); F. Hinterberger et al., Nucl. Phys. A106, 161 (1968).

[10]C. C. Chang et al., Phys. Rev. Lett. 34, 221 (1975); G. R. Satchler, Phys. Rep. 14, 97 (1974); F. E. Bertrand, Annu. Rev. Nucl. Sci. 26, 457 (1976).

[11]J. Blisplinghoff et al., Nucl. Phys. A269, 147 (1976).

[12]B. L. Cohen et al., Phys. Rev. 118, 499 (1960); E. W.

Hamburger et al., ibid. 121, 1143 (1961); G. Bahr and D. Trautmann, Phys. Rep. 25C, 293 (1976).

[13]L. Jarczyk et al., Phys. Lett. 39B, 191 (1972); O. F. Nemets et al., Yad. Fiz. 1, 1014 (1965) [Sov. J. Nucl. Phys. 1, 722 (1965)]; 4, 370 (1967); V. A. Pollitzer et al., Helv. Acta 41, 439 (1968).

[14]R. Serber, Phys. Rev. 72, 1008 (1947).

[15]J. R. Wu, Ph.D. Thesis, University of Maryland 1977 (unpublished).

[16]J. R. Wu, C. C. Chang and H. D. Holmgren, Phys. Rev. C (to be published).

[17]J. R. Wu and C. C. Chang, Phys. Rev. C 16, 1812 (1977).

[18]J. R. Wu and C. C. Chang, Phys. Rev. C 17, 1540 (1978).

[19]C. K. Cline, Nucl. Phys. A210, 590 (1973).

[20]F. D. Becchetti, Jr., and G. W. Greenless, Phys. Rev. 182, 1190 (1969); C. M. Perey and F. G. Perey, Nucl. Data Tables 13, 293 (1974).

[21]J. R. Huizenga and G. Igo, Nucl. Phys. 29, 462 (1962).

[22]D. B. Beard and A. McClellan, Phys. Rev. 140, B888 (1965).

[23]G. Harrison, Ph.D. Thesis, University of Maryland 1972 (unpublished); O. Aspelund et al., Nucl. Phys. A253, 263 (1975); F. Hinterburger, et al., ibid. A111, 265 (1968); G. Duhamel et al., ibid. A174, 485 (1971).